

Local and nonlocal spin Seebeck effect in lateral Pt-Cr₂O₃-Pt devices at low temperatures

Cite as: APL Mater. 9, 021122 (2021); doi: 10.1063/5.0037860

Submitted: 17 November 2020 • Accepted: 1 February 2021 •

Published Online: 22 February 2021



Prasanta Muduli,^{1,a)} Richard Schlitz,¹ Tobias Kosub,² René Hübner,² Artur Erbe,² Denys Makarov,² and Sebastian T. B. Goennenwein¹

AFFILIATIONS

¹Institut für Festkörper- und Materialphysik and Würzburg-Dresden Cluster of Excellence ct.qmat, Technische Universität Dresden, 01062 Dresden, Germany

²Helmholtz-Zentrum Dresden-Rossendorf e.V., Institute of Ion Beam Physics and Materials Research, 01328 Dresden, Germany

^{a)}Author to whom correspondence should be addressed: prasanta_kumar.muduli@tu-dresden.de

ABSTRACT

We have studied thermally driven magnon spin transport (spin Seebeck effect, SSE) in heterostructures of antiferromagnetic α -Cr₂O₃ and Pt at low temperatures. Monitoring the amplitude of the local and nonlocal SSE signals as a function of temperature, we found that both decrease with increasing temperature and disappear above 100 K and 20 K, respectively. Additionally, both SSE signals show a tendency to saturate at low temperatures. The nonlocal SSE signal decays exponentially for intermediate injector–detector separation, consistent with magnon spin current transport in the relaxation regime. We estimate the magnon relaxation length of our α -Cr₂O₃ films to be around 500 nm at 3 K. This short magnon relaxation length along with the strong temperature dependence of the SSE signal indicate that temperature-dependent inelastic magnon scattering processes play an important role in the intermediate range magnon transport. Our observation is relevant to low-dissipation antiferromagnetic magnon memory and logic devices involving thermal magnon generation and transport.

© 2021 Author(s). All article content, except where otherwise noted, is licensed under a Creative Commons Attribution (CC BY) license (<http://creativecommons.org/licenses/by/4.0/>). <https://doi.org/10.1063/5.0037860>

Recently, substantial scientific effort has focused on harnessing spin currents without Joule heating for low-dissipation information processing.¹ In magnetic materials, the spin current (i.e., the directed propagation of spin angular momentum) can be either due to electron spin or due to bosonic quasiparticle excitations of the magnetic order parameter called magnons. The realization of magnon spin currents in electrically insulating materials with a large bandgap is advantageous since they prevent energy dissipation due to ohmic losses owing to the electronic motion. Moreover, the spin propagation length of electronic spin currents is relatively short, typically ranging from nanometers in ferromagnetic metals up to micron length scales in very pure non-magnetic metals at low temperatures.² Magnon spin currents, on the other hand, can travel distances up to several micrometers in magnetic insulators.³ Magnons can be excited in magnetic insulators via numerous methods, e.g., magnetically using microwave-frequency AC magnetic fields (coherent magnons in the GHz range), thermally via the spin Seebeck effect (incoherent magnons in the THz range),⁴ and electrically using a low-frequency AC or DC electric current in a neighboring heavy metal with large spin Hall angle, such as platinum.³

Although the initial study of magnon spin currents was focused on ferromagnetic insulators, recently, antiferromagnetic insulators (AFIs) have moved into the focus of magnonics research due to their abundance in nature, better scalability in nanodevices with minimal cross-talk, immunity against magnetic field perturbations, and orders of magnitude faster magnetization dynamics at the terahertz frequency range.^{5–8} Magnon spin current transport has been demonstrated in many antiferromagnetic insulators, such as NiO,^{9,10} CoO,¹¹ α -Fe₂O₃,¹² MnPS₃,¹³ and Cr₂O₃.¹⁴ Additionally, the absence of dipole–dipole interactions makes axially symmetric AFIs the ideal materials for the realization of magnon Bose–Einstein condensates (BEC)^{15,16} and magnon spin superfluidity, i.e., a long-range propagating Goldstone mode arising from the spontaneous breaking of U(1) symmetry.^{17–19} All these recent studies on magnon spin transport in antiferromagnets have led to a new frontier research field called *antiferromagnetic magnonics* as a subfield of spintronics.

One fascinating effect hinging on thermally excited magnon spin transport is the so-called spin Seebeck effect (SSE). The spin Seebeck effect refers to the generation of magnon spin currents by a

temperature gradient applied across a magnetic material.⁴ The SSE is manifested as an electric voltage in an adjacent heavy metal layer in which the thermally driven spin current is converted into a charge current by the inverse spin Hall effect (ISHE).²⁰ Originally, it was assumed that AFIs will not exhibit a finite SSE due to the lack of a net magnetization and the particular properties of magnon modes in AFIs. More specifically, in a uniaxial AFI with two magnetic sublattices, there will be two degenerate magnon modes that produce spin currents in opposite directions under a thermal gradient such that the net spin current cancels out. However, the degeneracy of the two modes can be lifted by a magnetic field or even a spin flop transition to a ferromagnetic-like state, or by inversion symmetry breaking at an interface, resulting in finite SSE response.^{21,22} Such a magnetic field-induced SSE has been recently observed in various AFIs such as Cr_2O_3 ,^{23,24} MnF_2 ,²⁵ and FeF_2 .²⁶ Moreover, indication of magnon spin superfluidity has been recently reported in Cr_2O_3 .¹⁹

In this paper, we focus on local and nonlocal SSE experiments in antiferromagnetic $\alpha\text{-Cr}_2\text{O}_3$ thin films for small injector–detector separation. We perform magnetic-field-orientation-dependent local and nonlocal SSE measurements by rotating an external magnetic field of constant magnitude in three orthogonal planes. By monitoring the amplitude of the local and nonlocal voltage modulations as a function of different parameters, such as the temperature and the spatial separation between the injector–detector Pt strips, we probe the spin transport via antiferromagnetic magnons. From these data, we extract the magnon spin diffusion length (l_m) in the diffusive transport regime at low temperatures. We show that although in the long-distance regime, superfluid spin transport might be realized, the intermediate-distance range is dominated by magnon diffusion, while the superfluid contribution is not detectable.

We use $\alpha\text{-Cr}_2\text{O}_3$ for our spin transport experiments since this material is one of the best studied AFIs with uniaxial anisotropy.^{27,28} The single crystal $\alpha\text{-Cr}_2\text{O}_3$ has a hexagonal (corundum) crystal structure with the $R\bar{3}c$ space group. The magnetic structure is dictated by layers of Cr^{3+} ions ($S = 3/2$) with an antiparallel sublattice spin alignment along the $[0001]$ axis such that in the (0001) plane, all Cr^{3+} ions belong to the same antiferromagnetic sublattice. Previous spin transport experiments have shown that the transmission of the spin current in Cr_2O_3 depends on its Néel vector orientation.^{14,29,30} The spin transmission is completely blocked below the Néel temperature (T_N) if the Néel vector \mathbf{N} of Cr_2O_3 (oriented along the $[0001]$ easy axis) is aligned perpendicular to the polarization of the injected spin current. Interestingly, Cr_2O_3 abruptly becomes a good spin conductor above T_N .¹⁴

The $\alpha\text{-Cr}_2\text{O}_3$ thin films were grown by magnetron sputter deposition (base pressure: 10^{-7} mbar, Ar sputter pressure: 10^{-3} mbar, and deposition rate: 0.04 nm/s) of a pure Cr_2O_3 target material (Robeko GmbH & Co. KG). To initiate the crystallization of $\alpha\text{-Cr}_2\text{O}_3$, single-crystalline Al_2O_3 (0001) substrates (Crytec GmbH) were heated to 850°C before deposition. The $\alpha\text{-Cr}_2\text{O}_3$ thin films were deposited at 700°C . The samples were capped *in situ* with a sputtered 3-nm-thick Pt layer at lower temperatures of $\approx 100^\circ\text{C}$ (deposition rate 0.1 nm/s). The films were found to be of high crystallinity and atomically smooth with single lattice steps in height at the boundary between plateaus, as discussed in more detail in Ref. 31. Structural characterization reveals (0001)-oriented growth, assuring an out-of-plane easy axis of the Néel vector for

250-nm-thick films. From cross-sectional transmission electron microscopy (TEM) [see Fig. 1(a)], the films were found to be granular with about 50-nm-sized columnar grains with very high crystallinity within each grain (see Sec. S1 of the [supplementary material](#) for further TEM characterization). Note also from Fig. 1(a) that the $\text{Cr}_2\text{O}_3/\text{Pt}$ interface has a certain morphological roughness, probably due to strain. However, we confirmed via energy-dispersive x-ray spectroscopy (EDXS) in scanning TEM (STEM) mode that there is no Pt diffusion into the Cr_2O_3 film (see Fig. S2 of the [supplementary material](#)). In our TEM and STEM-EDXS analyses, we also found no hints of surface oxidation or other signs for damage to the Cr_2O_3 surface due to Pt deposition.

Multiple lateral devices were fabricated on one and the same sample with electron beam lithography and Ar-ion milling (see Sec. S2 of the [supplementary material](#) for further fabrication details). Figure 1(b) shows a schematic of a Pt– Cr_2O_3 –Pt nonlocal device with two Pt strips, one acting as the injector and the other as the detector. The length and width of the platinum strips for all devices studied here are approximately $L = 145\ \mu\text{m}$ and $W = 500\ \text{nm}$, respectively. We prepared a series of nonlocal Pt– Cr_2O_3 –Pt devices with an edge-to-edge spacing d_{nl} between the two Pt strips varying from $0.4\ \mu\text{m}$ to $4\ \mu\text{m}$. Local and nonlocal voltage measurements were performed using a quasi-DC method applying a DC current $I = 150\ \mu\text{A}$ through one of the Pt strips and periodically reversing its direction. We measure both symmetric $V_{loc(nl)}^s = (V_{loc(nl)}(I+) + V_{loc(nl)}(I-))/2$ and antisymmetric $V_{loc(nl)}^{as} = (V_{loc(nl)}(I+) - V_{loc(nl)}(I-))/2$ voltages for both local (loc) and nonlocal (nl) measurement configurations. The antisymmetric voltage $V_{loc(nl)}^{as}$ and symmetric voltage

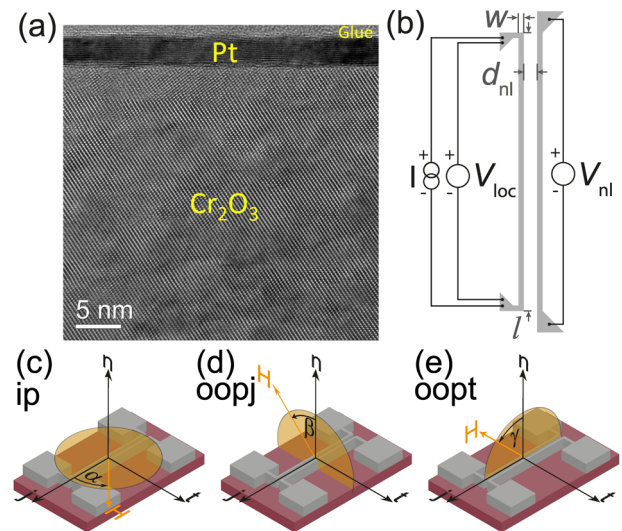


FIG. 1. (a) Cross-sectional high-resolution TEM image of the Cr_2O_3 –Pt bilayer film. A high crystalline quality of the $\alpha\text{-Cr}_2\text{O}_3$ individual grains and a sharp Cr_2O_3 –Pt interface are evident. (b) Device schematics with local and nonlocal measurement configurations. An electric current I is applied at one Pt strip, and voltages can be detected at the same strip (locally) or at the other strip (nonlocally). [(c)–(e)] Device schematics with different external magnetic field \mathbf{H} (yellow arrow) rotation planes: (c) ip-rotation in the \mathbf{j} – \mathbf{t} plane with angle $\alpha = \angle \mathbf{jH}$ (α -rotation), (d) oopj-rotation in the \mathbf{t} – \mathbf{n} plane with angle $\beta = \angle \mathbf{nH}$ (β -rotation), and (e) oopt-rotation in the \mathbf{n} – \mathbf{j} plane with angle $\gamma = \angle \mathbf{nH}$ (γ -rotation).

$V_{loc}^s(nl)$ are equivalent to the first harmonic voltage (V^{1f}) and second harmonic voltage (V^{2f}) measured with an AC lock-in technique, respectively.^{12,32–36}

Driving a charge current through Pt can generate magnons in α -Cr₂O₃ via two different mechanisms, electrical and thermal.^{33,37} Due to the spin Hall effect inside Pt, a transverse spin current is generated orthogonal to the current direction, and a spin accumulation μ_s with spin polarization along the \mathbf{t} axis builds up at the Pt–Cr₂O₃ interface. When a magnetic field is applied, it can cause canting of the Cr³⁺ moments in the two different magnetic sublattices, producing a canted moment \mathbf{M}_{cnt} . Nonequilibrium magnon spin accumulation is created inside α -Cr₂O₃ via exchange interaction at the interface if the spin accumulation direction μ_s is not orthogonal to \mathbf{M}_{cnt} . Additionally, Joule heating of the injector charge current creates a temperature gradient ∇T in α -Cr₂O₃, which thermally generates nonequilibrium magnons through the SSE. The nonequilibrium magnons diffuse inside α -Cr₂O₃ and can be detected by the other (or the same) Pt strip. Hereby, because of the ISHE, the magnon spin current is converted into a charge current in Pt, producing a voltage in open-circuit condition. The electrically generated magnon voltage signal is contained in the antisymmetric part $V_{loc(nl)}^{as}$ of the measured voltage, which is linear with current.^{12,35} The voltage produced thermally by the SSE is quadratic in current and is contained in the symmetric part $V_{loc(nl)}^s$ (see Sec. S3 of the [supplementary material](#) for further details).

We measured both the antisymmetric $V_{loc(nl)}^{as}$ and the symmetric $V_{loc(nl)}^s$ voltages in the local and nonlocal configurations, while the external magnetic field \mathbf{H} was rotated in three different orthogonal planes, as depicted in Figs. 1(c)–1(e). The three orthogonal rotation planes of the external magnetic field \mathbf{H} are (1) ip-rotation in the \mathbf{j} – \mathbf{t} plane with angle $\alpha = \angle \mathbf{jH}$ (α -rotation), (2) oopj-rotation in the \mathbf{t} – \mathbf{n} plane with angle $\beta = \angle \mathbf{nH}$ (β -rotation), and (3) oopt-rotation in the \mathbf{n} – \mathbf{j} plane with angle $\gamma = \angle \mathbf{nH}$ (γ -rotation). For the antisymmetric signal $V_{loc(nl)}^{as}$, no modulation was observed at any temperature and magnetic field (see Sec. S5 of the [supplementary material](#) for further details). This can be rationalized considering that in our measurement configuration, the spin accumulation direction μ_s (in-plane) is perpendicular to the Néel vector \mathbf{N} (out-of-plane). Therefore, the electrical excitation of magnons is inefficient.^{14,29} In the following, we therefore focus only on the symmetric voltage $V_{loc(nl)}^s$, which includes the thermally generated SSE signal.

Figure 2 summarizes the angular dependence of the local and nonlocal SSE voltages for all three rotation planes at 10 K. A constant, angle-independent voltage offset was subtracted from all the data (see Sec. S4 of the [supplementary material](#) for further details). The angular dependence was measured applying a magnetic field $\mu_0 H = 2$ T, large enough to create a small canting of the Cr³⁺ moments along the field direction. A clear modulation of the local voltage can be observed for the α - and β -rotation planes in Fig. 2(a). The angular dependence follows a $\sin(\alpha, \beta)$ dependence. This agrees with the expected behavior for the spin Seebeck effect³⁸ and thus confirms the notion that the symmetric V_{loc}^s arises due to magnons excited thermally. In contrast, if the magnons were generated electrically, one would expect a $\sin^2(\alpha, \beta)$ behavior.³³ In a simple microscopic picture, we thus assume that if the magnetic field is applied perpendicular to the [0001] easy axis (along \mathbf{n}), a finite canting is induced, and consequently, a finite magnetization \mathbf{M}_{cnt} appears in

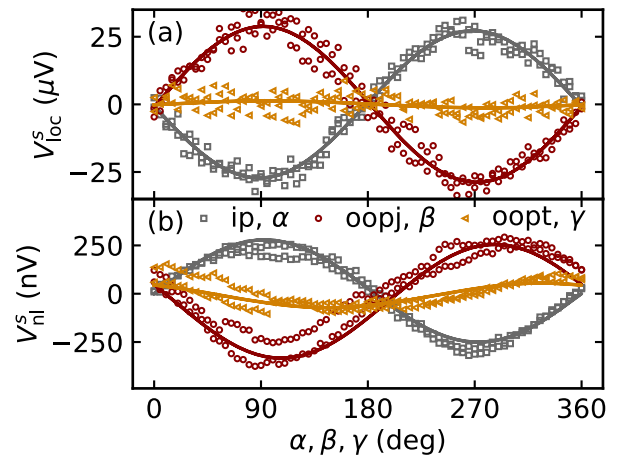


FIG. 2. Magnetic-field-orientation-dependent evolution of the voltage symmetric in current $V_{loc(nl)}^s$ (i.e., SSE voltage) measured at 10 K for the device with $d_{nl} = 0.4 \mu m$. A magnetic field of $\mu_0 H = 2$ T was hereby used to induce a canted moment \mathbf{M}_{cnt} in α -Cr₂O₃. (a) The local SSE voltage signal V_{loc}^s shows a clear modulation only for α - and β -rotations. (b) The same $\sin(\alpha, \beta)$ modulation with opposite sign is observed for the nonlocal SSE voltage signal V_{nl}^s . Note that an average offset voltage signal was subtracted.

α -Cr₂O₃. The induced magnetization, in turn, gives rise to a finite spin Seebeck effect, which is maximum if $\mathbf{H} \parallel \mathbf{t}$, i.e., when the spin accumulation μ_s direction and the induced magnetization \mathbf{M}_{cnt} align (anti-)parallel. Consequently, the SSE vanishes, and no voltage modulation can be observed in the γ -rotation plane, where the induced magnetization \mathbf{M}_{cnt} is always perpendicular to μ_s (or \mathbf{t}) and thus cannot generate a voltage in the given geometry (no magnons can be excited or detected).

For the nonlocal signal, a slightly different behavior is observed, as shown in Fig. 2(b). Although the signal magnitude is smaller, a clear modulation of the nonlocal SSE voltage (V_{nl}^s) is observed during magnetic field rotation in the α - and β -plane. The signal is similar to the local V_{loc}^s and follows a $\sin(\alpha, \beta)$ dependence, however, with opposite sign. In thermally excited magnon transport experiments in ferrimagnetic YIG, the sign of the nonlocal SSE signal reverses at a critical distance d_{rev} . The critical distance d_{rev} is determined by the thickness of the magnetic insulator and the interfacial spin transparency of the injector (detector) contacts.^{36,37,39,40} In our case, we thus infer that the injector–detector separation d_{nl} is larger than d_{rev} in all the devices since we invariably observe the same sign in V_{nl}^s , which is opposite to the sign of V_{loc}^s .

Figure 3 shows the nonlocal SSE signal at several temperatures, measured with an applied magnetic field of $\mu_0 H = 2$ T rotated in-plane (α -rotation). A significant change of the local and nonlocal signal magnitudes as a function of temperature is evident from the data. Both the local and nonlocal signals show a stronger modulation for lower temperatures, while the modulation seems to disappear at higher temperatures. The amplitude of the voltage modulation $A_{loc(nl)}^s$ represents the SSE signal without thermoelectric offsets. Expressing our SSE signal magnitude in a nonlocal resistance (normalized to the wire length), we obtain values of $\approx 0.23 \frac{V}{\mu m A^2}$ in good

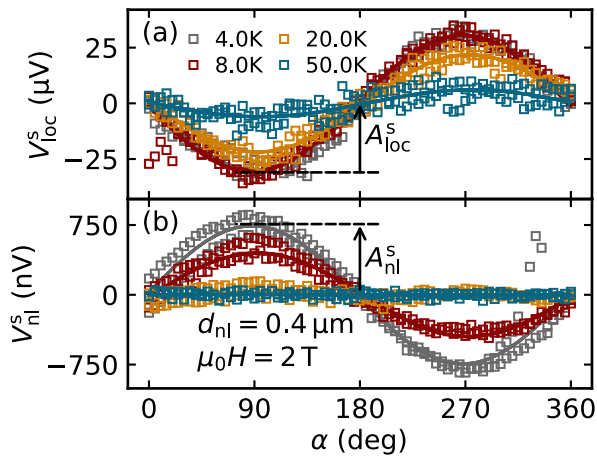


FIG. 3. The angle dependence of (a) the local SSE signal V_{loc}^s and (b) the nonlocal SSE signal V_{nl}^s is shown here for several temperatures between 4 K and 50 K for the device with $d_{nl} = 0.4 \mu\text{m}$. Here, $A_{loc(nl)}^s$ indicated by arrow represent the amplitude of SSE signal modulation. A clear increase of the amplitude of the SSE signal modulation $A_{loc(nl)}^s$ is evident toward lower temperatures. An average offset voltage independent of the magnetic field direction was subtracted from the data.

agreement with Yuan *et al.*¹⁹ (see Sec. S4 of the [supplementary material](#) for more details). To better compare the temperature evolution, the amplitudes of the voltage modulations $A_{loc(nl)}^s$ were extracted using a $\sin(\alpha)$ fit and compiled in Fig. 4. Although both the local and the nonlocal signals saturate at low temperatures, the local signal A_{loc}^s saturates already around 10 K, while the modulation in the nonlocal voltage A_{nl}^s does so only below 5 K. In addition, the modulation in the local SSE signal vanishes at around 100 K, whereas

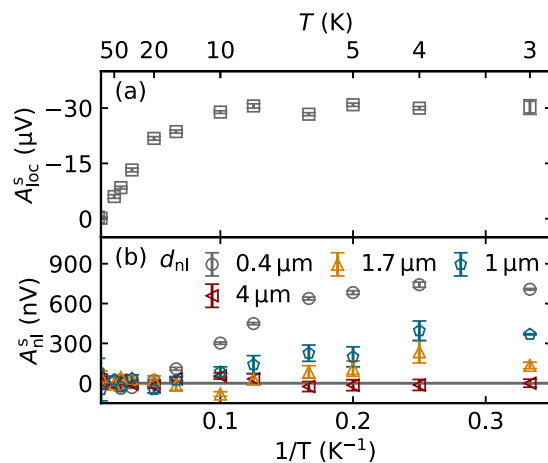


FIG. 4. The amplitudes of the $\sin\alpha$ -type modulation $A_{loc(nl)}^s$ in (a) the local and (b) the nonlocal SSE voltages as a function of reciprocal temperature for devices with different d_{nl} . A clear increase of the signals toward lower temperatures is evident. Interestingly, the local signal V_{loc}^s saturates already around 10 K, while the nonlocal signal V_{nl}^s saturates only around 5 K. The measurements were done with an in-plane magnetic field (α -rotation) $\mu_0H = 2 \text{ T}$.

the nonlocal SSE signal disappears already above 20 K. This suggests that although the general trends are similar, the detailed mechanisms relevant for the local and nonlocal SSE signals might differ. This can be understood considering that the thermal magnon excitation which is important for the local SSE signal, depends only on the temperature gradient ∇T_n underneath the injector, while the nonlocal signal is caused by magnon transport reaching far beyond the thermal gradient generated by the injected electrode.

So far, the exact nature of the increase of the thermal signal at low temperatures is not fully resolved. In Ref. 19, the low-temperature saturation in the nonlocal signal was attributed to a spin-superfluid ground state in the antiferromagnetic Cr_2O_3 , resulting from spontaneous breaking of the uniaxial symmetry. However, a similar behavior was also observed in Pt-YIG-Pt lateral devices, where a spin-superfluid ground state cannot be realized.⁴¹ Furthermore, in MnF_2 -Pt bilayers, the temperature dependence of the SSE signal shows a magnetic-field-dependent peak around $T \approx 7 \text{ K}$, which approximately matches the peak in thermal conductivity of MnF_2 .²⁵ In the case of Cr_2O_3 , a peak in thermal conductivity was observed for $T \approx 30 \text{ K}$.²³ Taken together, the low-temperature SSE response in antiferromagnets is far from well understood and requires further investigation.

Finally, we measured the evolution of the nonlocal SSE signal A_{nl}^s as a function of the injector-detector separation d_{nl} , as shown in Fig. 5. Beyond $d_{nl} = 4 \mu\text{m}$, we could not measure A_{nl}^s accurately anymore as the nonlocal voltage reached the noise level of the nanovoltmeter, and the signal-to-noise ratio becomes too small. Therefore, we focus only on the “small-distance” regime here. The length scale for the magnon spin current can be estimated from this A_{nl}^s vs d_{nl} data considering a one-dimensional spin diffusion model that describes the decay as³³

$$A_{nl}^s = C \exp\left(-\frac{d_{nl}}{l_m}\right), \quad (1)$$

where l_m is the magnon spin diffusion length and C is a constant independent of d_{nl} . We find that this simple exponential decay of the signal (red line) fits best to the measured data, and we estimate

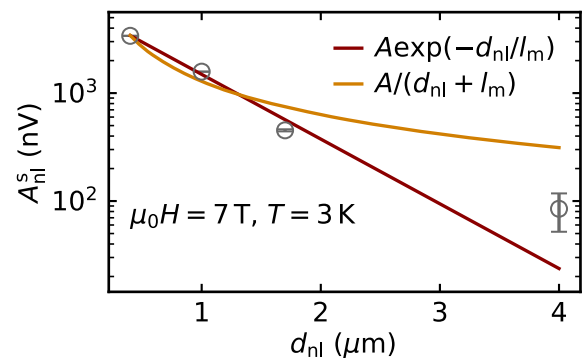


FIG. 5. The nonlocal SSE signal decreases for increasing injector-detector separation d_{nl} . Hereby, the decay is better described by an exponential, rather than an algebraic decay, as discussed in more detail in the text. The data were taken with an applied magnetic field of $\mu_0H = 7 \text{ T}$ at 3 K. We estimate a characteristic magnon decay length $l_m \approx 500 \text{ nm}$ under these conditions.

$l_m = 500$ nm at 3 K. This is quite small compared to the magnon spin diffusion length in the ferrimagnetic insulator YIG, where $l_m = 40$ μm at $T = 3.5$ K was reported using a similar nonlocal method.⁴⁰ This is also quite small compared to the magnon spin diffusion length in other antiferromagnets such as $\alpha\text{-Fe}_2\text{O}_3$ with $l_m = 9$ μm at 200 K.¹² In previous spin transport experiments in Cr_2O_3 thin films, Yuan *et al.*¹⁹ reported a very large $l_m = 16.3$ μm and assumed a spin-superfluid ground state to be realized in Cr_2O_3 . However, short (<10 nm) spin decay lengths through AFIs were observed in vertical (longitudinal geometry) spin transport devices.⁴²

In magnon spin transport experiments in YIG, three distinct transport regimes have been identified. For very short distances ($d \ll l_m$), the magnon signals typically drop faster than the exponential decay [Eq. (1)].^{37,40} Thereafter, for intermediate distances, an exponential decay is observed.³³ This regime is called the “exponential regime” or “relaxation regime.” Beyond this intermediate regime, A_{nl}^S shows a geometrical decay as $A_{nl}^S \sim \frac{1}{d_{nl}^2}$.⁴⁰ In this geometrical-decay regime, the signal is controlled by the temperature gradient ∇T present close to the detector, which also generates a magnon spin current that contributes to the measured nonlocal SSE signal. The good match of A_{nl}^S to Eq. (1) shown in Fig. 5 indicates that the spin signal in our case is dominated by magnon relaxation rather than diffusive transport.

In case of a spin-superfluid ground state, the nonlocal signal was predicted to follow a decay of the form^{17,19}

$$A_{nl}^S \sim \frac{1}{d_{nl} + l_m}. \quad (2)$$

As evident from Fig. 5, in our case, the exponential decay given by Eq. (1) fits much better to the data than an algebraic decay given by Eq. (2).

The relatively short magnon relaxation length along with the strong temperature dependence observed in our experiment suggests that temperature-dependent inelastic magnon scattering processes play an important role in long-range magnon transport through antiferromagnets.^{22,43} Note that from our previous structural and magnetic characterization of $\alpha\text{-Cr}_2\text{O}_3$ thin films (see Sec. S1 of the supplementary material), we have found that our films are of high crystalline quality but granular with a typical grain size of ~ 50 nm. In addition, they contain magnetic domains of typical dimension ~ 230 nm.^{31,44,45} The similar scale of the magnon spin relaxation length l_m and domain size suggests that inelastic magnon scattering processes from uncompensated magnetic moments at the grain boundaries or antiferromagnetic domain walls significantly impact or even dominate magnon transport in our $\alpha\text{-Cr}_2\text{O}_3$ thin films.^{46,47} Note that also in YIG, the magnon spin diffusion length depends strongly on the crystalline quality and texture. For example, at room temperature, $l_m = 38$ nm for sputtered YIG,⁴⁸ $l_m = 140$ nm for pulsed-laser-deposited YIG,⁴⁹ and $l_m = 9.4$ μm for liquid-phase-epitaxy YIG were observed.³³

In summary, we performed a detailed study of thermally excited magnon transport in antiferromagnetic $\alpha\text{-Cr}_2\text{O}_3$ thin films using a nonlocal device geometry. No direct electronic excitation of magnons could be observed, while a clear voltage signal arising from thermally generated magnons was picked up in the symmetric voltage. We found that the thermally generated local and nonlocal

voltages, measured while rotating a magnetic field of constant magnitude in three orthogonal planes, follow $\sin(\alpha)$ or $\sin(\beta)$ dependencies, as expected for the SSE. Temperature-dependent measurements showed that the SSE signals increase with decreasing temperature and saturate at very low temperatures. Finally, we estimated the length scale over which the thermally generated magnons diffuse by measuring the nonlocal SSE voltage signal as a function of the spatial separation of the injector and detector Pt strips. We conclude that magnon transport in our $\alpha\text{-Cr}_2\text{O}_3$ thin films is governed mainly by relaxation processes with a characteristic magnon spin diffusion length of $l_m = 500$ nm. The comparatively short magnon spin diffusion length and the strong temperature dependence of both the local and nonlocal SSE signals suggest that inelastic magnon scattering processes at the grain boundary or antiferromagnetic domain walls dominate the magnon transport at short distances in our samples. Our findings can inspire antiferromagnetic magnonic devices, such as non-volatile memory storage, logic gates, analog data processing, and quantum computing.

See the [supplementary material](#) for further details of TEM characterization (S1), device fabrication (S2), current dependence of the nonlocal signal (S3), thermoelectric offsets (S4), angle dependence of the antisymmetric voltage (S5), field dependence of the SSE signal (S6), and temperature dependence of Pt (S7).

We acknowledge funding from the Würzburg-Dresden Cluster of Excellence ct.qmat (EXC 2147, Project ID 390858490). We also acknowledge financial support from the Deutsche Forschungsgemeinschaft through SFB 1143/C08 and SPP 1538 [Project Nos. GO 944/4, TH1399/5, MA5144/9-1, MA5144/24-1, and MA5144/22-1 and Helmholtz Association of German Research Centres in the frame of the Helmholtz Innovation Lab “FlexiSens” (HIL-A04)]. Furthermore, the use of the HZDR Ion Beam Center TEM facilities is gratefully acknowledged. We also thank R. Aniol for TEM specimen preparation and T. Schönherr for technical support during ebl fabrication of devices.

DATA AVAILABILITY

The data that support the findings of this study are available from the corresponding author upon reasonable request.

REFERENCES

- ¹A. V. Chumak, V. I. Vasyuchka, A. A. Serga, and B. Hillebrands, *Nat. Phys.* **11**, 453 (2015).
- ²J. Bass and W. P. Pratt, *J. Phys.: Condens. Matter* **19**, 183201 (2007).
- ³Y. Kajiwara, K. Harii, S. Takahashi, J. Ohe, K. Uchida, M. Mizuguchi, H. Umezawa, H. Kawai, K. Ando, K. Takanashi, S. Maekawa, and E. Saitoh, *Nature* **464**, 262 (2010).
- ⁴K. Uchida, S. Takahashi, K. Harii, J. Ieda, W. Koshibae, K. Ando, S. Maekawa, and E. Saitoh, *Nature* **455**, 778 (2008).
- ⁵V. Baltz, A. Manchon, M. Tsoi, T. Moriyama, T. Ono, and Y. Tserkovnyak, *Rev. Mod. Phys.* **90**, 015005 (2018).
- ⁶T. Jungwirth, X. Marti, P. Wadley, and J. Wunderlich, *Nat. Nanotechnol.* **11**, 231 (2016).
- ⁷T. Jungwirth, J. Sinova, A. Manchon, X. Marti, J. Wunderlich, and C. Felser, *Nat. Phys.* **14**, 200 (2018).
- ⁸J. Železný, P. Wadley, K. Olejník, A. Hoffmann, and H. Ohno, *Nat. Phys.* **14**, 220 (2018).

- ⁹W. Lin, K. Chen, S. Zhang, and C. L. Chien, *Phys. Rev. Lett.* **116**, 186601 (2016).
- ¹⁰D. Hou, Z. Qiu, and E. Saitoh, *NPG Asia Mater.* **11**, 35 (2019).
- ¹¹Q. Li, M. Yang, C. Klewe, P. Shafer, A. T. N'Diaye, D. Hou, T. Y. Wang, N. Gao, E. Saitoh, C. Hwang, R. J. Hicken, J. Li, E. Arenholz, and Z. Q. Qiu, *Nat. Commun.* **10**, 5265 (2019).
- ¹²R. Lebrun, A. Ross, S. A. Bender, A. Qaiumzadeh, L. Baldrati, J. Cramer, A. Brataas, R. A. Duine, and M. Kläui, *Nature* **561**, 222 (2018).
- ¹³W. Xing, L. Qiu, X. Wang, Y. Yao, Y. Ma, R. Cai, S. Jia, X. C. Xie, and W. Han, *Phys. Rev. X* **9**, 011026 (2019).
- ¹⁴Z. Qiu, D. Hou, J. Barker, K. Yamamoto, O. Gomonay, and E. Saitoh, *Nat. Mater.* **17**, 577 (2018).
- ¹⁵S. O. Demokritov, V. E. Demidov, O. Dzyapko, G. A. Melkov, A. A. Serga, B. Hillebrands, and A. N. Slavin, *Nature* **443**, 430 (2006).
- ¹⁶D. A. Bozhko, A. A. Serga, P. Clausen, V. I. Vasyuchka, F. Heussner, G. A. Melkov, A. Pomyalov, V. S. L'vov, and B. Hillebrands, *Nat. Phys.* **12**, 1057 (2016).
- ¹⁷S. Takei, B. I. Halperin, A. Yacoby, and Y. Tserkovnyak, *Phys. Rev. B* **90**, 094408 (2014).
- ¹⁸E. B. Sonin, *Adv. Phys.* **59**, 181 (2010).
- ¹⁹W. Yuan, Q. Zhu, T. Su, Y. Yao, W. Xing, Y. Chen, Y. Ma, X. Lin, J. Shi, R. Shindou, X. C. Xie, and W. Han, *Sci. Adv.* **4**, eaat1098 (2018).
- ²⁰J. Sinova, S. O. Valenzuela, J. Wunderlich, C. H. Back, and T. Jungwirth, *Rev. Mod. Phys.* **87**, 1213 (2015).
- ²¹S. M. Rezende, R. L. Rodríguez-Suárez, and A. Azevedo, *Phys. Rev. B* **93**, 014425 (2016).
- ²²S. A. Bender, H. Skarsvåg, A. Brataas, and R. A. Duine, *Phys. Rev. Lett.* **119**, 056804 (2017).
- ²³S. Seki, T. Ideue, M. Kubota, Y. Kozuka, R. Takagi, M. Nakamura, Y. Kaneko, M. Kawasaki, and Y. Tokura, *Phys. Rev. Lett.* **115**, 266601 (2015).
- ²⁴J. Li, C. B. Wilson, R. Cheng, M. Lohmann, M. Kavand, W. Yuan, M. Aldosary, N. Agladze, P. Wei, M. S. Sherwin, and J. Shi, *Nature* **578**, 70 (2020).
- ²⁵S. M. Wu, W. Zhang, A. Kc, P. Borisov, J. E. Pearson, J. S. Jiang, D. Lederman, A. Hoffmann, and A. Bhattacharya, *Phys. Rev. Lett.* **116**, 097204 (2016).
- ²⁶J. Li, Z. Shi, V. H. Ortiz, M. Aldosary, C. Chen, V. Aji, P. Wei, and J. Shi, *Phys. Rev. Lett.* **122**, 217204 (2019).
- ²⁷S. Foner, *Phys. Rev.* **130**, 183 (1963).
- ²⁸T. Nagamiya, K. Yosida, and R. Kubo, *Adv. Phys.* **4**, 1 (1955).
- ²⁹J. Qin, D. Hou, Y. Chen, E. Saitoh, and X. Jin, *J. Magn. Magn. Mater.* **501**, 166362 (2020).
- ³⁰R. Schlitz, T. Kosub, A. Thomas, S. Fabretti, K. Nielsch, D. Makarov, and S. T. B. Goennenwein, *Appl. Phys. Lett.* **112**, 132401 (2018).
- ³¹P. Appel, B. J. Shields, T. Kosub, N. Hedrich, R. Hübner, J. Fassbender, D. Makarov, and P. Maletinsky, *Nano Lett.* **19**, 1682 (2019).
- ³²S. T. B. Goennenwein, R. Schlitz, M. Pernpeintner, K. Ganzhorn, M. Althammer, R. Gross, and H. Huebl, *Appl. Phys. Lett.* **107**, 172405 (2015).
- ³³L. J. Cornelissen, J. Liu, R. A. Duine, J. B. Youssef, and B. J. van Wees, *Nat. Phys.* **11**, 1022 (2015).
- ³⁴B. L. Giles, Z. Yang, J. S. Jamison, and R. C. Myers, *Phys. Rev. B* **92**, 224415 (2015).
- ³⁵M. Althammer, *J. Phys. D: Appl. Phys.* **51**, 313001 (2018).
- ³⁶K. Ganzhorn, T. Wimmer, J. Cramer, R. Schlitz, S. Geprägs, G. Jakob, R. Gross, H. Huebl, M. Kläui, and S. T. B. Goennenwein, *AIP Adv.* **7**, 085102 (2017).
- ³⁷J. Shan, L. J. Cornelissen, N. Vlietstra, J. Ben Youssef, T. Kuschel, R. A. Duine, and B. J. van Wees, *Phys. Rev. B* **94**, 174437 (2016).
- ³⁸K. Uchida, M. Ishida, T. Kikkawa, A. Kirihara, T. Murakami, and E. Saitoh, *J. Phys.: Condens. Matter* **26**, 343202 (2014).
- ³⁹X. J. Zhou, G. Y. Shi, J. H. Han, Q. H. Yang, Y. H. Rao, H. W. Zhang, L. L. Lang, S. M. Zhou, F. Pan, and C. Song, *Appl. Phys. Lett.* **110**, 062407 (2017).
- ⁴⁰J. Shan, L. J. Cornelissen, J. Liu, J. B. Youssef, L. Liang, and B. J. van Wees, *Phys. Rev. B* **96**, 184427 (2017).
- ⁴¹K. Oyanagi, T. Kikkawa, and E. Saitoh, *AIP Adv.* **10**, 015031 (2020).
- ⁴²H. Wang, C. Du, P. C. Hammel, and F. Yang, *Phys. Rev. B* **91**, 220410 (2015).
- ⁴³R. E. Troncoso, S. A. Bender, A. Brataas, and R. A. Duine, *Phys. Rev. B* **101**, 054404 (2020).
- ⁴⁴T. Kosub, M. Kopte, F. Radu, O. G. Schmidt, and D. Makarov, *Phys. Rev. Lett.* **115**, 097201 (2015).
- ⁴⁵T. Kosub, M. Kopte, R. Hühne, P. Appel, B. Shields, P. Maletinsky, R. Hübner, M. O. Liedke, J. Fassbender, O. G. Schmidt, and D. Makarov, *Nat. Commun.* **8**, 13985 (2017).
- ⁴⁶E. G. Tveten, A. Qaiumzadeh, and A. Brataas, *Phys. Rev. Lett.* **112**, 147204 (2014).
- ⁴⁷A. Ross, R. Lebrun, O. Gomonay, D. A. Grave, A. Kay, L. Baldrati, S. Becker, A. Qaiumzadeh, C. Ulloa, G. Jakob, F. Kronast, J. Sinova, R. Duine, A. Brataas, A. Rothschild, and M. Kläui, *Nano Lett.* **20**, 306 (2020).
- ⁴⁸H. Wu, C. H. Wan, X. Zhang, Z. H. Yuan, Q. T. Zhang, J. Y. Qin, H. X. Wei, X. F. Han, and S. Zhang, *Phys. Rev. B* **93**, 060403 (2016).
- ⁴⁹A. Kehlberger, U. Ritzmann, D. Hinzke, E.-J. Guo, J. Cramer, G. Jakob, M. C. Onbasli, D. H. Kim, C. A. Ross, M. B. Jungfleisch, B. Hillebrands, U. Nowak, and M. Kläui, *Phys. Rev. Lett.* **115**, 096602 (2015).